ACS NANO

www.acsnano.org

ARTICLE

Self-Adaptive Electrochemistry of Phosphate Cathodes toward Improved Calcium Storage

Shuhan Jin, Ruohan Yu,* Junjun Wang, Lianmeng Cui, Meng Huang, Lei Zhang,* and Qinyou An*

Cite This: *ACS Nano* 2024, 18, 28246–28257

Read Online

ACCESS | Metrics & More | Article Recommendations | Supporting Information

ABSTRACT: Polyanion phosphates exhibit great potential as calcium-ion battery (CIB) cathodes, boasting high working voltage and rapid ion diffusion. Nevertheless, they frequently suffer from capacity decay with irreversible phase transitions; the underlying mechanisms remain elusive. Herein, we report an adaptively layerized structure evolution from discrete $NaV_2O_2(PO_4)_2F$ nanoparticles (NPs) to interconnected $VOPO_4$ nanosheets (NSs), triggered by electrochemical (de)-calcification, leading to an improvement in Ca^{2+} storage performance. This electrochemistry-driven self-adapted layerization occurs over approximately 200 cycles, during which NPs undergo a "deform/merge-layerization" process, transitioning from a three-dimensional to a two-dimensional atomic structure, with a distinct 0.68 nm lattice spacing. The transition mechanism is demonstrated to be linked to the gradual separation of structural Na^+ and F^-. The resultant $VOPO_4$ NSs exhibit exceptional Ca^{2+} diffusion kinetics (3.19×10^{-9} cm^2 s^{-1}, currently the optimal value among inorganic cathode materials for CIBs), enhanced capacity (~100 mA h g^{-1}), longevity (over 1000 cycles at 50 mA g^{-1}), and high rate (84% retention rates when increasing current density from 50 to 200 mA g^{-1}). Employing advanced electron microscopy, this study reveals an electrochemical activation-induced structure evolution at the atomic level, providing valuable insights into the design of high-performance CIB cathodes.

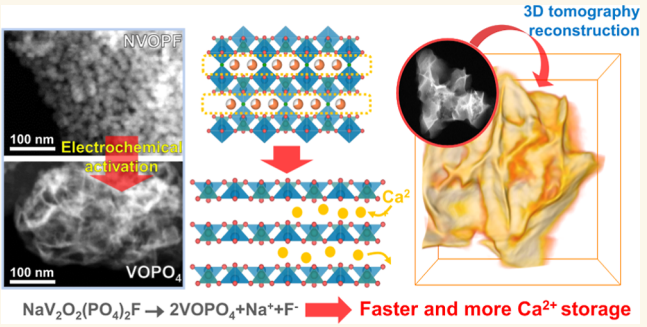

KEYWORDS: *Ca-ion batteries, cathode materials, reaction mechanism, electrochemical activation, structure transformation*

INTRODUCTION

Multivalent-ion batteries, such as those based on Zn^{2+}, Mg^{2+}, Ca^{2+}, and Al^{3+}, have attracted significant attention due to their high energy storage capability and safety. The multielectron process of polyvalent metals is expected to push through the energy density limit of secondary batteries compared to monovalent-ion systems.[1,2] Among multivalent-ion batteries, calcium-ion batteries (CIBs) are particularly promising, owing to the low standard electrode potential of Ca^{2+}/Ca (−2.87 V vs SHE)[3] and weak polarization strength of Ca^{2+} (10.4),[4,5] enabling higher output voltage and improved rate performance. Calcium's abundance in the earth's crust and seawater, along with its dendrite-free deposition,[6] makes CIBs an attractive, safe, and cost-effective solution for commercial energy storage.

Cathode materials are essential for the energy density of CIBs. Recent studies have investigated various nonaqueous CIB cathode materials, including Prussian blue analogues,[7,8] transition-metal oxides,[9−13] phosphates,[14,15] and organic compounds.[16] These materials often possess a layered structure that facilitates Ca^{2+} insertion/extraction. However, the larger size and higher charge of Ca^{2+} can easily destabilize the cathode structure, resulting in poor cycling performance.[11,13] Thus, developing cathode materials that can withstand the structural changes associated with Ca^{2+} insertion/extraction is crucial for advancing the CIB industry.

Polyanion phosphate cathodes, especially those with LISICON and NASICON structures, have gained significant interest due to their rapid ion transfer kinetics, high working voltage, and lattice stability in Li^+ and Na^+ batteries.[17,18] With the rise of CIBs, researchers have sought to adapt these materials to this emerging field. However, the larger ionic radius of Ca^{2+} compared to Li^+ and Na^+ presents a formidable challenge to maintaining the structural integrity of polyanion phosphates during repeated insertion/extraction.[19] Despite extensive efforts to enhance their resilience and accommodate (de)calciation, such as regulating the proportion and content of different elements in the structure[20,21] and the synthesis of

Received: June 29, 2024
Revised: September 19, 2024
Accepted: September 25, 2024
Published: October 3, 2024

https://doi.org/10.1021/acsnano.4c08704
ACS Nano 2024, 18, 28246−28257

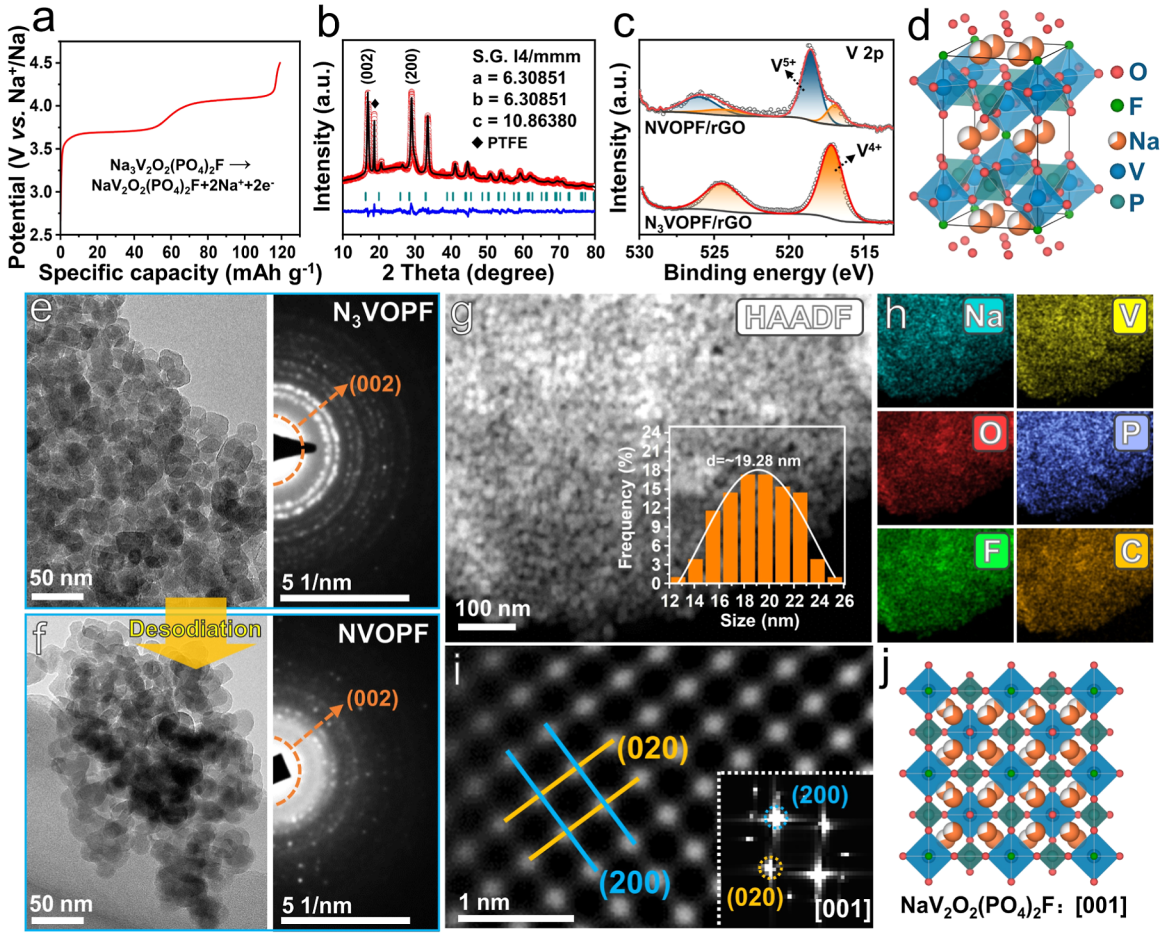

Figure 1. Structural characterizations of $NaV_2O_2(PO_4)_2F$ as a preactivated cathode material. (a) Galvanostatic charge/discharge profiles for the desodiation process of the N_3VOPF. (b) Rietveld refinement of NVOPF. (c) V 2p XPS spectra of N_3VOPF and NVOPF. (d) Crystal structure of NVOPF. TEM images and SAED patterns of (e) N_3VOPF and (f) NVOPF. (g) HAADF−STEM image, particle size distribution (inset of g), and corresponding (h) EDX mapping images of NVOPF. Atomic-resolution HAADF−STEM image of (i) NVOPF, corresponding FFT pattern (inset of i) and (j) crystal structure at the [001] orientation.

materials with expanded lattice parameters,[14] the structural integrity of conventionally prepared polyanion phosphates in chemical route remains insufficient for achieving stable cycling performance in CIBs.[22]

Electrochemical activation has emerged as a powerful method for fabricating unconventional materials with properties that are otherwise difficult to achieve through traditional synthesis routes.[23] Electrochemical conditions could enable spontaneous self-adaptive formation of thermodynamically unfavored/metastable structures, including ultrathin nanosheets (NSs),[24] ultrafine nanoparticles (NPs),[25,26] and open mesoporous structure,[27] often exhibiting significantly improved properties compared to their thermodynamically stable counterparts. Electrochemical structure activation is frequently mentioned to alter the properties of the electrode materials, such as introducing ion/electron conductive agents,[28] exposing additional storage sites,[29] or inducing new redox couples.[30] Nevertheless, a vast majority of them involve the consumption of the active ions for the proceedings of the activation process, leading to irreversible capacity loss.[13,31] Therefore, to effectively utilize the benefits of electrochemistry-induced structure activation in CIB electrode materials, it is crucial to identify suitable candidates that either exclude active Ca^{2+} from the activation process or employ them as catalysts during the structural transformation. Furthermore, a comprehensive investigation is urgently required to unravel the correlation between structural transformation and Ca^{2+} storage performance for the continued development of polyanion phosphate cathode materials in CIBs.

Herein, an electrochemical activation mechanism in $NaV_2O_2(PO_4)_2F$ (NVOPF) NPs is elucidated, resulting in enhanced Ca^{2+} storage properties. This transformation is characterized by a "deform/merge-layerization" process, initiated by repeated Ca^{2+} insertion/extraction. Over approximately 200 cycles, NVOPF undergoes a morphological evolution from three-dimensional (3D) discrete NPs to a two-dimensional (2D) interconnected network of $VOPO_4$ NSs. This structural transformation is driven by the progressive separation of structural Na^+ and F^-, occurring independently of Ca^{2+} consumption. The resultant $VOPO_4$ NSs demonstrate exceptional Ca^{2+} diffusion kinetics (3.19×10^{-9} cm^2 s^{-1}), representing the highest reported value among inorganic cathode materials for CIBs. Consequently, $VOPO_4$ NSs exhibit enhanced capacity (~100 mA h g^{-1}), long cycling stability (over 1000 cycles at 50 mA g^{-1}), and high rate (84% capacity retention under a current density increase from 50 to 200 mA g^{-1}). Utilizing advanced electron microscopy techniques, this study provides atomic-level insights into electrochemical structure activation, offering valuable guidance for the development of high-performance CIB cathodes.

https://doi.org/10.1021/acsnano.4c08704
ACS Nano 2024, 18, 28246−28257

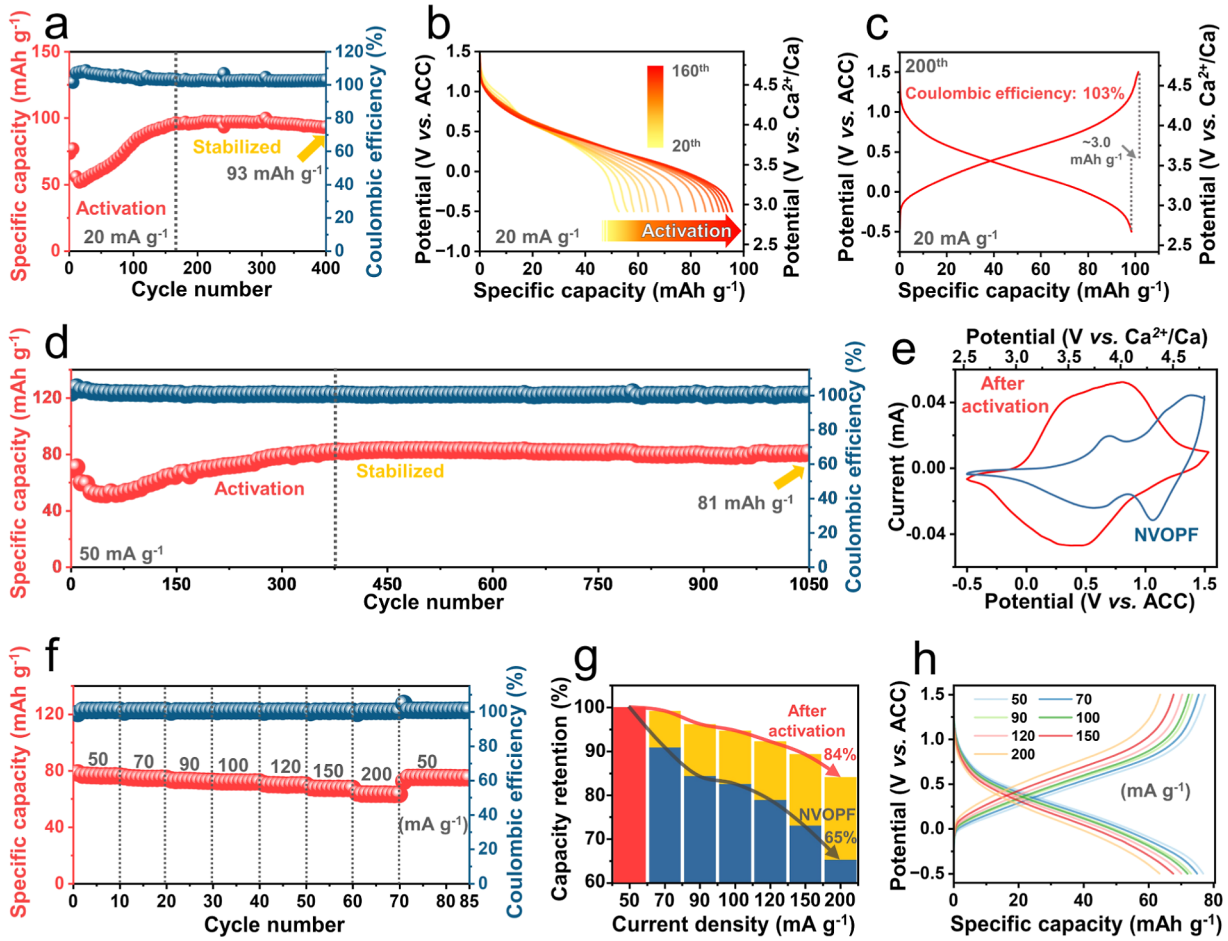

Figure 2. Improved calcium storage performance from electrochemical activation. (a) Cycling performance of NVOPF at 20 mA g^{-1} and representative (b) discharge profiles after different cycles. (c) Charge/discharge profile of the 200th cycle. (d) Cycling performance of NVOPF at 50 mA g^{-1}. (e) CV curves of the NVOPF before and after activation at a scan rate of 0.2 mV s^{-1}. (f) Rate performance after activation. (g) Capacity retention of NVOPF at different rates before (blue column) and after (orange column) activation. (h) Representative charge/discharge profiles from the rate performance after activation.

RESULTS AND DISCUSSION

Structural Characterizations of NVOPF as a Preactivated Cathode Material. NASICON structured NVOPF NPs were chosen as the pre-electrochemically activated cathode material. To gain such a material, Na-rich $Na_3V_2O_2(PO_4)_2F$ (N_3VOPF) NPs were synthesized as a precursor utilizing a facile hydrothermal method, while reduced graphene oxide (rGO) was added to improve the conductivity and electrochemical kinetic. Then, part of the Na^+ was removed through in situ desodiation to make room for the subsequent Ca^{2+} insertion/extraction (Figure 1a). We have confirmed the removal of active Na^+ through comparing the Rietveld refinement of X-ray diffraction (XRD) patterns of these two phases (Figures S1, 1b, and Tables S1 and S2). We have revealed the detailed content changes of two Na^+ sites: 8h and 8j sites.[32] Analysis of Na^+ occupancy in the 8h and 8j sites revealed a decreasing trend, with partial removal from the 8h sites and complete extraction from the 8j sites. This suggests that Na^+ at the 8h sites are electrochemically inert and serve as structural Na^+.[33] Meanwhile, the peak merging phenomenon in the XRD patterns, where the peak of the (101) plane merges with the (002), while the peak of the (103) plane merges with the (200), indicating successful removal of a portion of the active Na^+. Moreover, the increase in the lattice parameter *c* from 10.6341 to 10.8638 Å after desodiation further supports the extraction of active Na^+.[34]

The valence states of vanadium(V) in N_3VOPF and NVOPF were analyzed through X-ray photoelectron spectroscopy (XPS). As depicted in Figure 1c, the V in N_3VOPF exists in a tetravalent state (V^{4+}), whereas the appearance of V^{5+} in NVOPF confirms the successful desodiation process.[35] A comparative examination of the full XPS spectra (Figure S2) also reveals a decrease in the Na^+ content. The crystal structure of NVOPF exhibited a "pseudolayers" structure as depicted in Figure 1d: pairs of [VO5F] octahedrons share corner F atoms that is bonded to two structural Na^+ along the *c*-direction. The Raman spectrum suggest the enrichment of [PO4] within the structure (Figure S3).[36]

Transmission electron microscopy (TEM) and selected area electron diffraction (SAED) images were employed to compare the morphologies and crystal structures of N_3VOPF (Figure 1e) and NVOPF (Figure 1f). The morphology of NVOPF remains consistent with that of N_3VOPF. rGO enhances the conductivity on the surface of the NVOPF NPs (Figure S4). High-resolution TEM (HRTEM) images reveal the (002) plane of N_3VOPF and NVOPF (Figure S5), the increased lattice distance indicates the partial removal of the Na^+,[37] which matches well with the Rietveld refinement of XRD results. The high-angle annular dark-field (ADF)−

https://doi.org/10.1021/acsnano.4c08704
ACS Nano 2024, 18, 28246−28257

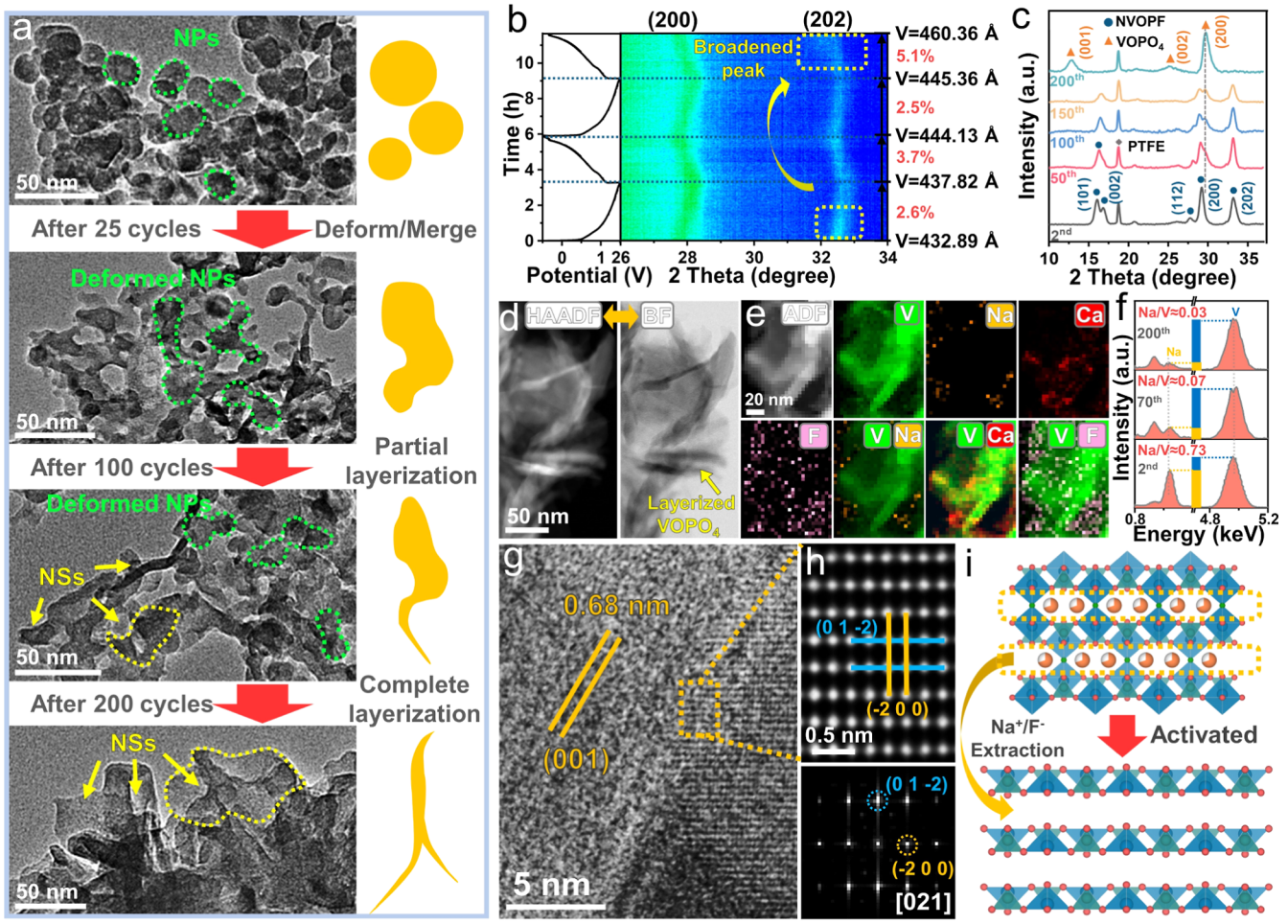

Figure 3. Nature of electrochemical activation-induced adaptive layerization. (a) TEM images after different cycles and schematic illustration showing the layerization process. (b) In situ XRD patterns and the corresponding charge/discharge profiles. (c) Ex situ XRD patterns at the decalciation state after different cycles. (d) HAADF/BF-STEM image of $VOPO_4$ NSs. (e) ADF−STEM image and corresponding EELS mapping images. (f) EDX spectra at the decalciation state after different cycles. (g) ADF−STEM images of $VOPO_4$. (h) Atomic-resolution HAADF images from labeled area in (g) and corresponding FFT patterns of $VOPO_4$. (i) Schematic illustration of structural evolution from NVOPF to $VOPO_4$.

scanning TEM (HAADF−STEM, Figure 1g) image indicates that N_3VOPF NPs are uniformly distributed with an average diameter of ∼19.28 nm. Energy-dispersive X-ray (EDX) mappings (Figure 1h) confirm the homogeneous signal distribution of Na, V, O, P, F, and C, which is similar to N_3VOPF (Figure S6). A comparative analysis of the normalized EDX spectra of N_3VOPF and NVOPF is provided in Figure S7, revealing a decrement in the Na signal intensity for NVOPF. Atomic-resolution HAADF−STEM image displays a periodic atomic arrangement from the internal structure of NVOPF, the corresponding fast Fourier transform (FFT) pattern suggest a [001] orientation of NVOPF (Figure 1i). This observation indicates that NVOPF maintains a tetragonal structure with space group *I*4/*mmm* (Figure 1j).

Improved Calcium Storage Performance from Electrochemical Activation. The electrochemical performance of NVOPF was evaluated using activated carbon cloth (ACC) as the counter electrode. This strategic approach effectively mitigates complexities associated with undesirable side reactions that may arise from the use of calcium metal.[8] The potential of the ACC was determined to be 3.168 V vs Ca^{2+}/Ca in $Ca(TFSI)_2$-propylene carbonate (PC)/ethyl carbonate (EC) electrolytes using a three-electrode system (Figure S8). It is worth noting that the current method for calculating the Coulombic efficiency (CE) for cathode materials in CIBs remains a topic of debate. Some researchers use the ratio of decalciation to calciation capacities,[14,38] while others employ the opposite.[4,5] Considering that CIB cathode materials, to date, do not inherently contain Ca and require an initial calciation process, the most rational and logical way for calculating CE should be to use the ratio of decalciation capacity to calciation capacity.

Figure 2a presents the cycling performance of the electrode material. The reported mass of the active material includes the rGO component. The capacity contribution from rGO within the same voltage window (−0.5 to 1.5 V vs ACC) is negligible (Figure S9). Initially, the specific capacity experiences a decline during the first few cycles, which is a typical observation in CIB polyanion cathode materials due to structure change.[19] However, it exhibits a subsequent and significant capacity increase, rising from 57 to 98 mA h g^{-1} over 160 cycles. This behavior suggests the presence of an activation process within the material potentially involving structural rearrangements or compositional changes that enhance the ability to store and release Ca^{2+}. Furthermore, the capacity stabilizes at 93 mA h g^{-1} for an additional 240 cycles, reaching a total of 400 cycles.

https://doi.org/10.1021/acsnano.4c08704
ACS Nano 2024, 18, 28246−28257

This extended stability implies that the activation process not only improves the capacity but also induces structural integrity within the material, enabling its ability to withstand repeated cycling without significant degradation.

Notably, the CE consistently exceeds 100% throughout the entire cycling process (Figure S10), particularly during the activation stage, where it reaches approximately 106%. This phenomenon indicates that the number of active ions extracted from the cathode during charge surpasses the number intercalated during the discharging process. Such behavior is different from the expected 1:1 ion transfer and suggests a more complex interplay of processes occurring within the electrode material. One explanation could involve the extraction of not only Ca^{2+} but also other cationic species present within the electrode material, leading to an excess of charge during discharge.

Figure 2b presents the representative galvanostatic discharge profiles of the electrode material. It is evident that the calciation slopes progressively shift toward lower potentials as the cycle number increases. This phenomenon indicates subtle changes in the electrode's electrochemical behavior as the capacity increases during the cycling process, suggesting a dynamic evolution of the material's structural or compositional properties during the activation process. Figure 2c presents a charge/discharge profile of the NVOPF material after activation at the 200th cycle. The discharge capacity attains a value of 98 mA h g^{-1}, accompanied by a CE of 103%. The average charge and discharge voltages are 3.64 and 3.42 V vs Ca^{2+}/Ca, respectively, which rank among the high values reported for CIB cathode materials.[5,21] Figure 2d illustrates the cycling performance at a current density of 50 mA g^{-1}. The capacity remained stable for more than 1000 cycles after activation, maintaining a value of 81 mA h g^{-1} for 1050 cycles. In addition, it is observed that NVOPF is capable of cycling 3000 times at 100 mA g^{-1} with a capacity maintaining at ~60 mA h g^{-1} (Figure S11). This capacity retention demonstrates the exceptional cycling stability of NVOPF. The cyclic voltammetry (CV) curves of NVOPF before and after activation reveal significant changes in its electrochemical behavior (Figure 2e). The electrochemical activation shifts these peaks to lower potentials but increases peak currents, suggesting the changes in electrochemical activity and reaction mechanism.

The activation process significantly enhances the NVOPF's rate capability, demonstrating its ability to maintain high capacity even at elevated current densities. As depicted in Figure 2f, specific capacities of 76.3, 75.7, 73.4, 72.3, 70.4, 68.2, and 64.2 mA h g^{-1} are achieved at current densities of 50, 70, 90, 100, 120, 150, and 200 mA g^{-1}, respectively. The capacity is restored to 75.4 mA h g^{-1} when the current density is again reduced to 50 mA g^{-1}. Furthermore, the capacity retention at higher current densities showcases the effectiveness of the activation process: compared to the capacity at 50 mA g^{-1}, the retention rates at 70, 90, 100, 120, 150, and 200 mA g^{-1} are 99.2%, 96.2%, 94.8%, 92.3%, 89.4%, and 84.1%, respectively, which indicates a substantial improvement over NVOPF before activation (Figures 2g and S12). The slopes in the charge/discharge curves shift to higher/lower potential (Figure 2h), indicative of a slight increase in polarization.[39]

Nature of Electrochemical Activation-Induced Adaptive Layerization. Ex situ TEM studies were conducted to explore the structural evolution process during the electrochemical activation (Figure 3a). It is observed that in the pristine state, NVOPF exhibits a discrete NPs morphology. After 25 cycles, the NPs are no longer spherical but become deformed, aggregated, and merged, like a pile of soft clay balls that have been pressed together. HRTEM shows that the deformed NPs are actually polycrystalline NVOPF (Figure S13). Such a polycrystalline process might be associated with the crystal pulverization/disintegration from the volume expansion/contraction during Ca^{2+} insertion/extraction.[40] After 100 cycles, we observed flake-like NSs formed within the deformed NPs and gradually became the dominant phase after 200 cycles. Such a layerization process should be attributed to the gradual formation of a new crystal phase with a layered atomic arrangement as the intrinsic structure evolution origin. Over 200 cycles, the pristine discrete NVOPF NPs have gradually become deformed/merged and eventually evolved into the interconnected NSs (Figure S14).

To further explore the crystalline nature of the generated layerized phase associated with the dynamic electrochemical activation process, in situ XRD was employed. Figure 3b presents the in situ XRD pattern of NVOPF during two cycles after the initial discharge. Throughout the charging process, the (200) and (202) diffraction peaks shift toward higher angles, which is attributed to the lattice contraction resulting from the extraction of Ca^{2+}. During the subsequent discharging process, these peaks return to their initial positions. The continuous changes in these peaks indicate that the Ca^{2+} storage mechanism proceeds via a single-phase insertion/extraction reaction.[41] Figures S15 presents the Rietveld refinement of XRD pattern and a structural schematic of the calciated state. The Rietveld refinement result presented in Table S3 reveals increases in the *a* and *b* lattice parameters and a decrease in the *c* parameter ($a = b = 6.36496$ Å, $c = 10.73254$ Å), suggesting the refilling of Ca^{2+} to the previously emptied Na^{+} sites. The observed decrease in lattice parameter *c* can be ascribed to the diminished electrostatic repulsion between adjacent O^{2-} layers. This reduction in interlayer repulsion stems from the progressive filling of Ca^{2+} layers, which effectively screens the negative charges on the oxygen ions. Conversely, the expansion of the lattice parameter *a* is attributed to the increase in the vanadium octahedra size upon electrochemical reduction of vanadium ions.[5] The EDX spectrum and mappings of the calciated state of NVOPF (Figures S16 and S17) exhibit a clear Ca signal, which also confirms the Ca^{2+} insertion.[22]

The unit cell volumes can also be calculated from the lattice parameters from the in situ XRD results. The cell volume demonstrates a volumetric expansion in the calciated state, which continues to increase in the subsequent cycle (Figure 3b). The volumetric expansion rate of the unit cell after calciation during the second cycle rises from 3.7 to 5.1%. This observation indicates that part of the structural deformation induced by Ca^{2+} insertion/extraction is irreversible, which explains the initial capacity decline in Figure 2a,d. Furthermore, compared with the initial state, the crystallinity of the (202) plane after the second discharge process is reduced (Figure S18), suggesting a poly crystallization process, which matches well with the TEM results (Figures 3a and S13).

Ex situ XRD was employed to investigate the electrochemically activated product. Figure 3c presents ex-situ XRD patterns of NVOPF at charged states after different cycles (corrected with the PTFE peak). It is observed that over 200 cycles, the peaks of the original NVOPF phase have gradually broadened/disappeared, while a set of new peaks emerge at

https://doi.org/10.1021/acsnano.4c08704
ACS Nano 2024, 18, 28246−28257

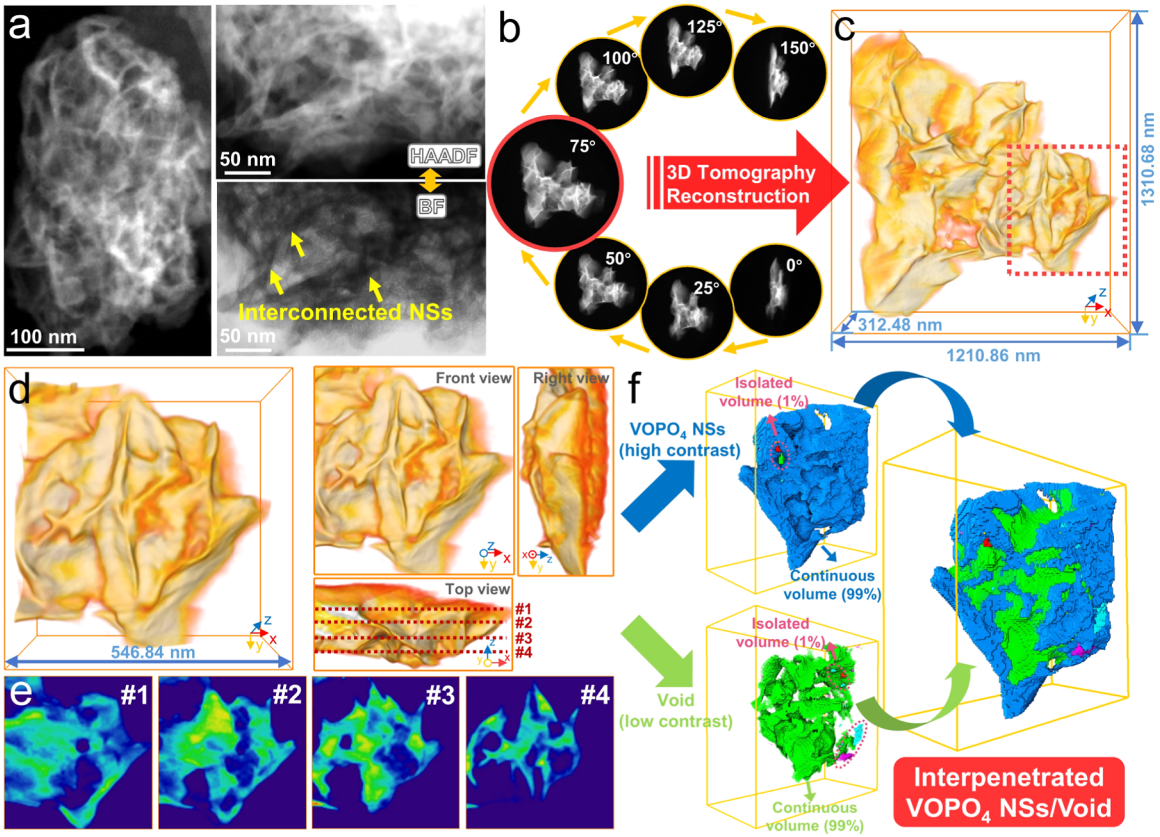

Figure 4. Interconnected structure characterization. (a) HAADF/BF−STEM images of $VOPO_4$ NSs in the charged state at the 200th cycle. (b) Representative STEM−HAADF images at different rotation angles and reconstructed $VOPO_4$ NSs. (c) Reconstructed $VOPO_4$ NSs model. (d) Extracted volume from area labeled by red dashed area in (c) and the corresponding front, top, and right views. (e) Representative ortho slices [*xy* planes, perpendicular to the *z*-axis at 25 (#1), 31 (#2), 37 (#3), and 43 (#4) nm] marked by the red dashed lines in (d). (f) Volumes from segmentation by contrast corresponding to $VOPO_4$ NSs (blue) and voids (green), respectively.

12.8, 25.2, and 29.7°, which are assigned to the (001), (002), and (200) planes of $VOPO_4$, respectively.[42] This observation demonstrates that NVOPF undergoes a complete transformation into $VOPO_4$ during the electrochemical activation process.

To further understand the structural characteristics of $VOPO_4$, we performed HAADF−STEM and EDX analyses. The HAADF−STEM and corresponding bright-field (BF)−STEM images clearly reveal the morphology of $VOPO_4$ (Figure 3d). Figure 3e presents the ADF−STEM image and the corresponding electron energy loss spectroscopy (EELS) mappings of V, Ca, Na, and F. The V-EELS signal is primarily localized throughout the interior region of the $VOPO_4$ NSs and aligns well with the bright contrast region in the ADF image. The Na-EELS mapping exhibits a strong signal in the dark contrast area of the ADF image, confirming the near-complete extraction of Na^+ from the structure. Conversely, the Ca-EELS signal is relatively weak and primarily distributed at the surface of the $VOPO_4$ NSs, suggesting the possible presence of Ca in the cathode-electrolyte interphase (CEI). Similarly, the F-EELS signal is predominantly located at the surface of the $VOPO_4$ NSs, indicating the migration of F^- from the inner region to the CEI at the surface.

To further confirm the extraction of Na^+, F^- from the structure, ex situ EDX spectra (Figure 3f), EDX mapping (Figures S19 and S20), and XPS (Figure S21) were conducted. Ex situ EDX spectra of the charged electrode were collected at the second, 70th, and 200th cycles (normalized by *V*−*K* peaks, Figure 3f). The decreasing Na content with an increasing cycle number indicates that structural evolution is accompanied by the continuous separation of Na^+. Since the F signal is too subtle to be detected by EDX, ex situ XPS analysis was conducted (Figure S21a), The F 1s XPS peak exhibited a shift toward higher energy (~0.5 eV) in the decalciated state after 200 cycles, suggesting a change in its chemical environment from structural F^- in NVOPF to a surface CEI component (Figure S21b). It is worth noting that structural Na^+ and F^- are closely bonded, which makes their simultaneous separation highly possible. This is further supported by the shift in the V 2p XPS spectra (Figure S21c), where the main V peak in $VOPO_4$ shows a 0.2 eV shift toward higher energy compared to the initial desodiated NVOPF, indicating the successful transformation from NVOPF to $VOPO_4$.[42,43] Consequently, the transformation can be described by the following equation

$$NaV_2O_2(PO_4)_2F \rightarrow 2VOPO_4 + Na^+ + F^-$$

Figures 3g and S22 depict the STEM images of $VOPO_4$ after charging, revealing the (001), (002), and (200) planes of $VOPO_4$. The atomic-resolution HAADF−STEM image (Figure 3h) displays a periodic atomic arrangement with the corresponding FFT pattern showing the vertically aligned (01−2) and (−200) planes, corresponding to the [021] orientation of $VOPO_4$. Figure 3i provides a schematic illustration of the structural evolution from NVOPF to $VOPO_4$. During the activation process, the separation of structural Na^+ and F^- induces a transformation from the

https://doi.org/10.1021/acsnano.4c08704
ACS Nano 2024, 18, 28246−28257

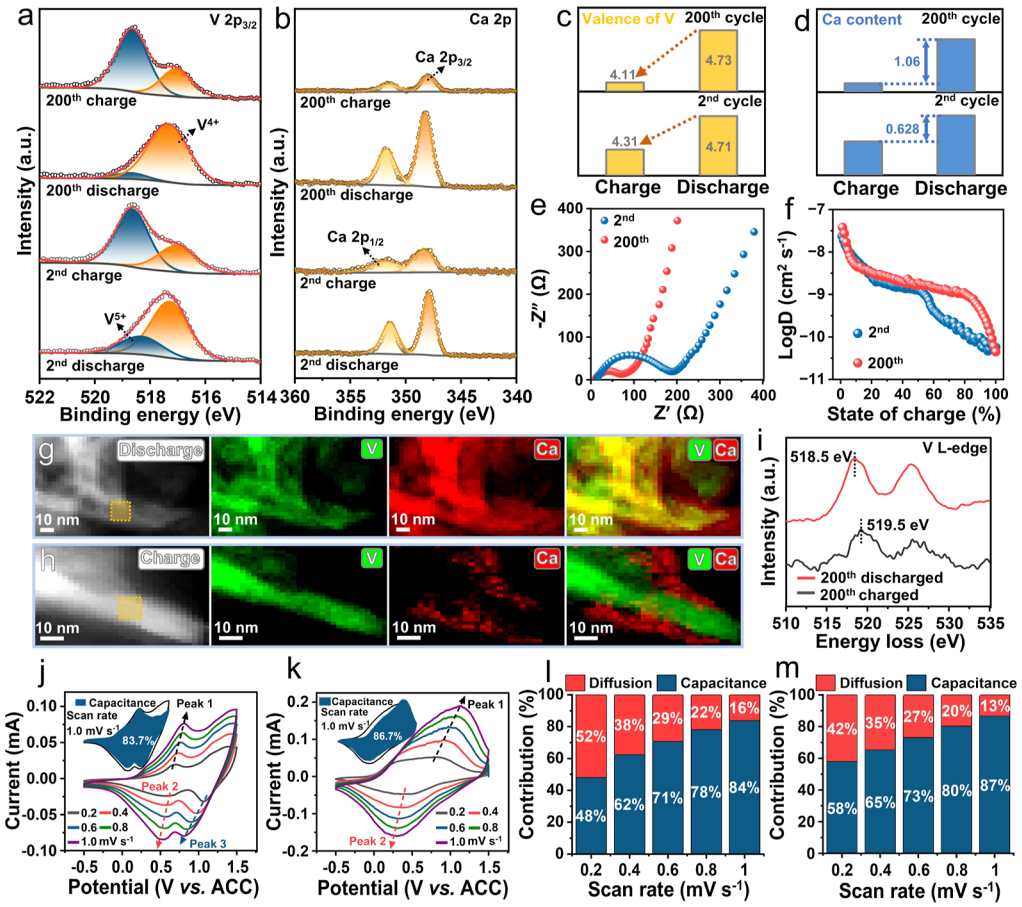

Figure 5. Advantages from electrochemical activation induced adaptive layerization. Ex situ XPS spectra of (a) V $2p_{3/2}$ and (b) Ca 2p at different states. Calculated (c) V valence states and (d) Ca content at charge/discharge state after different cycles. (e) EIS profiles and (f) calculated D_{Ca} from GITT curves after different cycles. ADF image and corresponding EELS mapping images at (g) discharge and (h) charge states after 200 cycles. (i) EELS spectra from labeled area in (g,h). The CV curves of (j) NVOPF and (k) $VOPO_4$ at different scan rates, and the insets are their calculated capacitive contribution to the charge storage at 1.0 mV s^{-1}, respectively. Percentage of the diffusion and capacitance contribution at different scan rates of (l) NVOPF and (m) $VOPO_4$.

NVOPF structure (tetragonal, space group *I*4/*mmm*) to the layered $VOPO_4$ structure (tetragonal, space group *P*4/*nmm*), ultimately leading to the "adaptive layerization" phenomenon. The layered $VOPO_4$ exhibits an enlarged interlayer lattice spacing (0.68 nm), which is beneficial for the stable insertion/extraction of Ca^{2+}.

The gradual separation of structural Na^+ provides a convincing explanation for the observed CE exceeding 100%. During the decalciation process, Na^+ migrate into the electrolyte, serving as a constant supplementary source of active positive charges (same as Ca^{2+}). This increased concentration of positive ions in the electrolyte attracts more $TFSI^-$ to the ACC anode (Figure S23), enhancing its capacity. Conversely, during the calciation process, the separated Na^+ are unable to reinsert into the NVOPF (Figure S24), resulting in a higher decalciation capacity compared to the calciation capacity. Notably, this phenomenon could be advantageous in certain scenarios, particularly when the counter electrode employed in CIBs can accommodate both Na^+ and Ca^{2+}. In such cases, the constant separation of Na^+ could potentially compensate for the CE loss at the anode, ultimately improving the overall energy density of the battery.

Interconnected Structure Characterization. Figure 4a displays the HAADF−STEM and corresponding BF−STEM images, revealing the interconnected network structure formed by $VOPO_4$ NSs. To further confirm the interconnected nature of the $VOPO_4$ NSs, 3D tomographic reconstruction was performed. 75 HAADF−STEM images were collected over a 150° range with a 2° interval for tomographic reconstruction (Supplementary Movie S1). The resulting reconstructed structural units and HAADF images at different rotation angles are shown in Figures 4b and S25. The reconstructed front view shape closely resembles the HAADF image captured at 75° angle, validating the effectiveness and authenticity of the reconstruction. Figures 4c and S25 present the front, right, and top views of the reconstructed unit. The length (*x*-axis), width (*z*-axis), and height (*y*-axis) of the bounding box are 1210.86, 312.48, and 1310.68 nm, respectively. Furthermore, the volume contrast is presented in the VolrenRed colormap, where high contrast (yellow) and low contrast (orange−red) within the structure correspond to $VOPO_4$ NSs and voids, respectively. To enhance visualization, ortho slicing and their dynamic process of reconstructed $VOPO_4$ NSs is presented (Supplementary Movie S2 and Figure S26). To better display the internal structure, the contrast of the ortho slices was converted to Physics colormap. Representative ortho slices marked with black pieces in the right view [*xy* plane, perpendicular to the *z*-axis at 25 (#1), 31 (#2), 37 (#3), and 43 (#4) nm] of the reconstructed unit demonstrate the interconnected nature of the ultrathin $VOPO_4$ NSs.

https://doi.org/10.1021/acsnano.4c08704
ACS Nano 2024, 18, 28246−28257

Subsequently, to further analyze the interconnected network structure, a subvolume extraction operation was performed on the reconstructed $VOPO_4$ NSs (Figure 4c). Figure 4d displays a magnified image of the region marked by the red dashed area in Figure 4c. The length (x-axis), width (z-axis), and height (y-axis) of the bounding box for the front, right, and top view images of the reconstructed structure are 546.84, 260.4, and 581.56 nm, respectively (Supplementary Movie S3). The internal structure of the ortho slices (Figure 4e) is also identified as continuous. Furthermore, as depicted in Figure 4f and Supporting Information, segmentation based on STEM−HAADF contrast was employed to separate high-contrast volumes ($VOPO_4$ NSs) from low-contrast volumes (voids). Figure S27 illustrates the separation process. The blue region represents continuous $VOPO_4$ NSs, while colors other than blue indicate isolated regions. Notably, over 99% of the volume is continuous (Figure S28a). Similarly, the majority of the voids (green region) are also continuous (Figure S28b). Moreover, the volume of voids accounts for 25% of the total volume, suggesting that this structural transformation is expected to prevent NP aggregation during cycling, thereby enhancing the material's activity and stability. Conclusively, the initially isolated NVOPF NPs bridged by weak physical attachment undergo a transformation into a continuous, integrated network of $VOPO_4$ NSs, which further accelerates Ca^{2+} transport.

Advantages Enabled by the Adaptive Layerization. Beyond the gradual separation of Na^+ acting as a constant supplementary source of active ions, enhancing the CE, the adaptive layerization process offers several additional advantages for calcium storage. These can be categorized into four key aspects: (I) increased calcium storage sites in the structure; (II) improved electron/Ca^{2+} diffusion kinetic; (III) enhanced reversibility for Ca^{2+} insertion/extraction; (IV) improved pseudocapacitance contribution, as elaborated below.

Layerized $VOPO_4$ Showed Increased Calcium Storage Sites in the Structure. XPS was employed to examine the chemical environment of Ca^{2+} in both charged and discharged states, aiming to elucidate the changes in the Ca^{2+} storage mechanism before and after electrochemical activation. Ex situ XPS analysis (Figure 5a) reveals the electrochemical reaction mechanism of $VOPO_4$ NSs and its comparison with NVOPF. Both NVOPF and $VOPO_4$ exhibit a similar tendency in the V valence state during charge and discharge. Upon discharging to −0.5 V, Ca^{2+} insertion leads to reduction of V^{5+} to V^{4+}. Conversely, charging to 1.5 V resulted in the oxidation of V^{4+} to V^{5+}.[44] Additionally, Ca 2p is detected in the discharged state, with a significantly decreased signal intensity observed after charging (Figure 5b).[9,10] Notably, $VOPO_4$ exhibited more sufficient Ca^{2+} extraction after charging compared to that of NVOPF.

Figure 5c,d presents a comparison of the calculated changes in the V valence state and Ca content during the second and 200th charge/discharge cycles. $VOPO_4$ displays a higher number of transferred electrons during the charge/discharge process compared to NVOPF (Figure 5c). Additionally, the difference in Ca content between the charged and discharged states of $VOPO_4$ is greater than that of NVOPF (Figure 5d), which matches well with the results in Figure 5c and provides crucial evidence for the capacity increase.

Layerized $VOPO_4$ Showed Improved Electron/Ca^{2+} Diffusion Kinetic. Electrochemical impedance spectroscopy (EIS) analysis was employed to investigate the charge transfer and ion diffusion kinetics before and after the electrochemical activation (Figure 5e). The reduced diameter of the high-frequency semicircle after 200 cycles (in the charged state) indicates a decrease in the charge transfer resistance. Additionally, the increased slope in the low-frequency region suggests enhanced Ca^{2+} diffusion kinetics.[45] To further determine the accurate Ca^{2+} diffusion coefficient and study the variation of the diffusion coefficient in the different discharge states, galvanostatic intermittent titration technique (GITT) was employed (Figure S29). Both NVOPF and $VOPO_4$ exhibited a gradual decrease in Ca^{2+} diffusion coefficient with increasing calciation depth (Figure 5f), potentially due to the reduction in available Ca^{2+} intercalation sites.[46] However, $VOPO_4$ demonstrated a notably higher Ca^{2+} diffusion coefficient at high calciation depths compared to that of NVOPF, which agrees well with the EIS results. This enhancement could be attributed to the increased lattice distance in $VOPO_4$, providing Ca^{2+} with a greater spatial mobility. Consequently, the average Ca^{2+} diffusion coefficient of $VOPO_4$ (3.19×10^{-9} cm^2 s^{-1}) is higher than that of NVOPF (2.37×10^{-9} cm^2 s^{-1}). It is worth mentioning that such electrochemical activation-induced $VOPO_4$ exhibits the highest Ca^{2+} diffusion coefficient among inorganic cathode materials for CIBs, surpassing typical values observed in other multivalent-ion battery cathode materials and even approaching those found in monovalent-ion battery cathode materials (Table S4).

Enhanced Reversibility for Ca^{2+} Insertion/Extraction Minimized the Consumption of Active Ca^{2+} and Maximized the Capacity. Figure 5g,h presents STEM−EELS mappings of $VOPO_4$ in charged and discharged states from representative regions (Figure S30). The Ca signal within $VOPO_4$ nearly disappears after charging, while the presence of Ca signals outside $VOPO_4$ may be attributed to Ca^{2+} in the CEI layer,[47,48] with minimal content as evidenced by the nearly absent peaks in the corresponding EELS spectra (Figure S30). After full discharge, an obvious Ca signal is observed within the host material.

EELS spectra reveal a shift in the V L_3-edge of $VOPO_4$ from 519.5 eV in the charged state to 518.5 eV in the discharged state (Figure 5i), confirming the reduction of V to a lower oxidation state upon Ca^{2+} insertion.[49] These EELS results demonstrate that the de(calciation) of $VOPO_4$ is highly reversible and is capable of fully extracting Ca^{2+} during the charge process, which minimized the consumption of active Ca^{2+} and maximized the capacity.

Increased Capacity from Pseudocapacitance Contribution. Multiscan rate CV tests were conducted to investigate the Ca^{2+} migration kinetics in NVOPF and $VOPO_4$ (Figure 5j,k). NVOPF exhibited one oxidation peak and two reduction peaks, with peak shape distortion and overlap at higher scan rates, suggesting an ongoing structural evolution. Conversely, $VOPO_4$ displayed two broad, stable redox peaks across all scan rates, confirming its excellent structural stability.

To further understand the diffusion mechanism, the relationship between peak current (i) and scan rate (v) was determined according to eq 1[50]

$$i = av^b \tag{1}$$

The slopes of the fitted lines in Figure S32 represent the b values for NVOPF and $VOPO_4$. The b values for the three peaks of NVOPF are 0.85, 0.8, and 0.58 (Figures S32a), indicating the coexistence of diffusion control and capacitive

https://doi.org/10.1021/acsnano.4c08704
ACS Nano 2024, 18, 28246−28257

behavior in the charge storage process.[9] The b values for the two peaks of $VOPO_4$ are 0.79 and 0.76 (Figures S32b), with the ion diffusion peak disappearing and capacitive control increasing. To analyze the proportion of capacitive contributions at different scan rates, eq 2 was used to assess the capacity ratio between capacitive (k_1v) and diffusion-controlled ($k_2v^{1/2}$) processes during cycling[51]

$$i = k_1v + k_2v^{1/2} \quad (2)$$

At a scan rate of 1 mV s^{-1}, the shaded area in the CV curve represents the capacitive contribution to charge storage, which is 83.7% for NVOPF (Figure 5j inset) and 86.7% for $VOPO_4$ (Figure 5k inset), indicating an enhanced pseudocapacitance in $VOPO_4$. For both NVOPF and $VOPO_4$, the capacitive contribution increased with increasing scan rates (Figure 5l,m), suggesting a dominant role of capacitive control in charge storage at higher scan rates.[52]

The adaptive structural transformation of NVOPF during electrochemical activation significantly enhances its calcium storage capabilities, resulting in improved capacity, cycle stability, and rate performance. This enhancement originates from two key factors: (i) the atomic arrangement transferred from a 3D framework to a 2D layered structure with increased interlayer lattice spacing and almost emptied interlayer structural Na^+ facilitates smoother and more sufficient Ca^{2+} insertion/extraction. (ii) The morphological transition from discrete 3D nanospheres to an interconnected network of 2D NSs provides shorter and continuous diffusion pathways, enabling faster kinetics for Ca^{2+} transport.

CONCLUSIONS

In summary, we reveal an electrochemically driven structural transformation in NVOPF, enhancing its Ca^{2+} storage capabilities. Over approximately 200 cycles, the discrete NVOPF NPs undergo a "deform/merge-layerization" process, transitioning from a 3D framework to a 2D interconnected network of $VOPO_4$ NSs with a layered structure. This transformation, triggered by repeated calcification-decalcination, involves the gradual separation of structural Na^+ and F^-, without consuming Ca^{2+}. The resulting 2D interconnected $VOPO_4$ NSs are expected to avoid aggregation of NPs and simultaneously promote Ca^{2+} transport during cycling. The resulting 2D interconnected $VOPO_4$ NSs facilitates Ca^{2+} transport, prevents NP aggregation, and offers increased active sites, which increased calcium storage sites, improved electron/Ca^{2+} diffusion kinetic, enhanced reversibility for Ca^{2+} insertion/extraction, and improved pseudocapacitance contribution, collectively contributing to advanced electrochemical performance. This study elucidates the distinctive calcium storage mechanism of polyanionic phosphates, offering valuable insights into the design and optimization of polyanionic phosphate cathodes for CIBs.

EXPERIMENTAL SECTION

Materials Synthesis. $Na_3V_2O_2(PO_4)_2$ (N_3VOPF) was synthesized through a hydrothermal method. First, solution A was prepared by dissolving 4.5 mmol of NaF and 3 mmol of $NH_4H_2PO_4$ in 15 mL of deionized water. In the meantime, solution B was prepared by dissolving 3 mmol of vanadyl acetylacetonate ($VO(acac)_2$) in a 50 mg suspension of GO dispersed in *N*,*N*-dimethylformamide suspension (2 mg g^{-1}). Second, solution A was poured into solution B to obtain solution C after 10 min of stirring. The obtained solution C was sealed in 100 mL Teflon-lined autoclaves and heated at 180 °C for 24 h. After natural cooling to room temperature, the obtained precipitations were centrifuged and washed with deionized water and ethanol for several times. Finally, the N_3VOPF cathode material was obtained after freeze-drying.

The prepared N_3VOPF was mixed with super P and poly(tetrafluoroethylene) PTFE binder (the mass ratio is 7:2:1) and then pressed into thin sheets using a Roller Press. The positive electrode sheet was obtained after being dried overnight at 70 °C. The mass loading of the active material was about 7−8 mg cm^{-2}. A sodium ion coin cell was assembled with the prepared cathode, separator (GF/A Whatman glass fiber), and Na metal anode and was charged to 4.5 V to obtain $NaV_2O_2(PO_4)_2$ (NVOPF). The electrolyte used in this work was 1 M $NaClO_4$ in EC/dimethyl carbonate (1:1 v/v ratio) with 5% fluoroethylene carbonate. Before being used as working electrodes in calcium-ion batteries, the desodiated electrodes were washed with anhydrous acetonitrile (ACN) several times and kept in a glovebox ($O_2 \leq 1$ ppm and $H_2O \leq 1$ ppm).

Material Characterization. In situ XRD measurements were performed using Bruker AXS D8 Advance powder X-ray diffractometer with a detector using Cu Kα X-ray source. Powder and ex situ XRD Rigaku MiniFlex600-C with a detector using a Cu Kα X-ray source. TEM, HRTEM, HAADF images, and EDX mappings were carried out using a Titan G2 60−300 microscope. Microstructural analysis was conducted using a double aberration-corrected FEI Titan Themis TEM instrument (Thermo Fisher) operated at 300 kV. HAADF−STEM imaging was performed with a probe convergence angle of 17.8 mrad, achieving a spatial resolution of 0.08 nm, and a probe current of ∼40 pA was used for EDX mapping imaging. For atomic resolution STEM imaging, the probe current was further reduced to ∼1 pA for minimized beam damage. The HAADF images were acquired using an annular-type STEM detector with a collection inner semiangle of 84 mrad. EELS data was acquired using a Gatan Quantum 965 GIF system with a beam current of ∼10 pA, simultaneously recording zero-loss, V L, and Ca L edges for calibration. Electron tomography was conducted using a Fischione tomography holder with a tilt range of ±80°, with reconstruction and visualization performed using Thermo Fisher 3D Inspect and Avizo software, respectively. Chemical state and elemental composition were determined via XPS using an ESCALAB 250Xi (Thermo-Fisher Scientific Co., USA). Raman spectroscopy used an excitation wavelength of 532 nm (Thermo-Fisher Scientific Co., USA).

Electrochemical Analysis. The pure rGO electrode was fabricated using a mixture of rGO powder, Super P, and PTFE binder in a weight ratio of 7:2:1. This mixture was then processed into a uniform film using a Roller Press, resulting in a mass loading of 7−8 mg cm^{-2}. The electrochemical performance of NVOPF cathode material was measured in 2016-type coin cells assembled with desodiated NVOPF as a cathode, GF/A Whatman glass fiber as a separator, and ACC as an anode in the glovebox. A PC/EC (1:1 v/v ratio) solution of 0.5 M $Ca(TFSI)_2$ was used as the electrolyte. The mass loadings of the cathode active material and ACC are about 7−8 and 16 mg cm^{-2}, respectively. The galvanostatic charge−discharge tests and GITT were carried out at a voltage window of −0.5 to 1.5 V vs ACC using LAND CT2001A and NEWARE multichannel battery testing systems. CV and EIS tests were collected from an electrochemical workstation (CORRTEST CS3105) under the alternating current ranging from 0.01 Hz to 10 kHz. All electrochemical tests were carried out at room temperature.

ASSOCIATED CONTENT

Data Availability Statement

All data needed to evaluate the conclusions in this paper are present in the paper or in the Supporting Information.

Supporting Information

The Supporting Information is available free of charge at https://pubs.acs.org/doi/10.1021/acsnano.4c08704.

Rietveld refinement and corresponding crystal structure scheme, HRTEM images, XPS spectra, Raman spectrum,

https://doi.org/10.1021/acsnano.4c08704
ACS Nano 2024, 18, 28246−28257

HAADF images, EDX mapping images, EDX spectra of N_3VOPF, NVOPF, and calciated NVOPF; CE, cycling performance, rate performance, GITT analysis, and multiscan CV analysis of NVOPF; HRTEM images, HAADF−STEM images of NVOPF in charged state at different cycles; ex situ XPS spectra and ex situ XRD patterns of NVOPF; STEM images, 3D reconstructed images, ADF images, and EELS spectra of $VOPO_4$; and schematic illustration of the charge/discharge process during electrochemical activation (PDF)

Rotation of the interconnected $VOPO_4$ NSs from HAADF−STEM images at various tilt angles (MP4)

Rotation and ortho slicing process of interconnected $VOPO_4$ NSs from 3D reconstruction (MP4)

Rotation and ortho slicing process of reconstructed $VOPO_4$ after subvolume extraction (MP4)

Rotation and ortho slicing process of $VOPO_4$ and voids components from contrast segmentation in 3D reconstruction (MP4)

AUTHOR INFORMATION

Corresponding Authors

Ruohan Yu − *Sanya Science and Education Innovation Park of Wuhan University of Technology, Sanya 572000, P. R. China*; Email: yuruohan@whut.edu.cn

Lei Zhang − *Sanya Science and Education Innovation Park of Wuhan University of Technology, Sanya 572000, P. R. China; State Key Laboratory of Advanced Technology for Materials Synthesis and Processing, Wuhan University of Technology, Wuhan 430070, P. R. China*; Email: zhanglei1990@whut.edu.cn

Qinyou An − *Sanya Science and Education Innovation Park of Wuhan University of Technology, Sanya 572000, P. R. China; State Key Laboratory of Advanced Technology for Materials Synthesis and Processing, Wuhan University of Technology, Wuhan 430070, P. R. China*; orcid.org/0000-0003-0605-4942; Email: anqinyou86@whut.edu.cn

Authors

Shuhan Jin − *Sanya Science and Education Innovation Park of Wuhan University of Technology, Sanya 572000, P. R. China; State Key Laboratory of Advanced Technology for Materials Synthesis and Processing, Wuhan University of Technology, Wuhan 430070, P. R. China*

Junjun Wang − *State Key Laboratory of Advanced Technology for Materials Synthesis and Processing, Wuhan University of Technology, Wuhan 430070, P. R. China*; orcid.org/0000-0001-6651-0204

Lianmeng Cui − *State Key Laboratory of Advanced Technology for Materials Synthesis and Processing, Wuhan University of Technology, Wuhan 430070, P. R. China*

Meng Huang − *Sanya Science and Education Innovation Park of Wuhan University of Technology, Sanya 572000, P. R. China*

Complete contact information is available at: https://pubs.acs.org/10.1021/acsnano.4c08704

Author Contributions

The manuscript was written through contributions of all authors. All authors have given approval to the final version of the manuscript.

Notes

The authors declare no competing financial interest.

ACKNOWLEDGMENTS

This work was supported by the Project of Sanya Yazhou Bay Science and Technology City (grant No. SCKJ-JYRC-2023-55), the National Natural Science Foundation of China (52172231, 52474333, and 22109123), and the Natural Science Foundation of Hubei Province (2022CFA087).

REFERENCES

(1) Wang, M.; Jiang, C.; Zhang, S.; Song, X.; Tang, Y.; Cheng, H. M. Reversible calcium alloying enables a practical room-temperature rechargeable calcium-ion battery with a high discharge voltage. *Nat. Chem.* **2018**, *10* (6), 667−672.

(2) Xiong, F.; Jiang, Y.; Cheng, L.; Yu, R.; Tan, S.; Tang, C.; Zuo, C.; An, Q.; Zhao, Y.; Gaumet, J. J.; et al. Low-strain TiP_2O_7 with three-dimensional ion channels as long-life and high-rate anode material for Mg-ion batteries. *Interdiscip. Mater.* **2022**, *1* (1), 140−147.

(3) Zhao-Karger, Z.; Xiu, Y.; Li, Z.; Reupert, A.; Smok, T.; Fichtner, M. Calcium-tin alloys as anodes for rechargeable non-aqueous calcium-ion batteries at room temperature. *Nat. Commun.* **2022**, *13* (1), 3849.

(4) Xu, X.; Duan, M.; Yue, Y.; Li, Q.; Zhang, X.; Wu, L.; Wu, P.; Song, B.; Mai, L. Bilayered $Mg_{0.25}V_2O_5{\cdot}H_2O$ as a Stable Cathode for Rechargeable Ca-Ion Batteries. *ACS Energy Lett.* **2019**, *4* (6), 1328−1335.

(5) Xu, Z. L.; Park, J.; Wang, J.; Moon, H.; Yoon, G.; Lim, J.; Ko, Y. J.; Cho, S. P.; Lee, S. Y.; Kang, K. A new high-voltage calcium intercalation host for ultra-stable and high-power calcium rechargeable batteries. *Nat. Commun.* **2021**, *12* (1), 3369.

(6) Pu, S. D.; Gong, C.; Gao, X.; Ning, Z.; Yang, S.; Marie, J.-J.; Liu, B.; House, R. A.; Hartley, G. O.; Luo, J.; Bruce, P. G.; Robertson, A. W. Current-Density-Dependent Electroplating in Ca Electrolytes: From Globules to Dendrites. *ACS Energy Lett.* **2020**, *5* (7), 2283−2290.

(7) Kuperman, N.; Padigi, P.; Goncher, G.; Evans, D.; Thiebes, J.; Solanki, R. High performance Prussian Blue cathode for nonaqueous Ca-ion intercalation battery. *J. Power Sources* **2017**, *342*, 414−418.

(8) Lipson, A. L.; Pan, B.; Lapidus, S. H.; Liao, C.; Vaughey, J. T.; Ingram, B. J. Rechargeable Ca-Ion Batteries: A New Energy Storage System. *Chem. Mater.* **2015**, *27* (24), 8442−8447.

(9) Wang, J.; Wang, J.; Jiang, Y.; Xiong, F.; Tan, S.; Qiao, F.; Chen, J.; An, Q.; Mai, L. $CaV_6O_{16}{\cdot}2.8H_2O$ with Ca^{2+} Pillar and Water Lubrication as a High-Rate and Long-Life Cathode Material for Ca-Ion Batteries. *Adv. Funct. Mater.* **2022**, *32* (25), 2113030.

(10) Zuo, C.; Xiong, F.; Wang, J.; An, Y.; Zhang, L.; An, Q. MnO_2 Polymorphs as Cathode Materials for Rechargeable Ca-Ion Batteries. *Adv. Funct. Mater.* **2022**, *32* (33), 2202975.

(11) Bu, H.; Lee, H.; Hyoung, J.; Heo, J. W.; Kim, D.; Lee, Y. J.; Hong, S.-T. $_2V_7O_{16}$ as a Cathode Material for Rechargeable Calcium-Ion Batteries: Structural Transformation and Co-Intercalation of Ammonium and Calcium Ions. *Chem. Mater.* **2023**, *35* (19), 7974−7983.

(12) Purbarani, M. E.; Hyoung, J.; Hong, S.-T. Crystal-Water-Free Potassium Vanadium Bronze ($K_{0.5}V_2O_5$) as a Cathode Material for Ca-Ion Batteries. *ACS Appl. Energy Mater.* **2021**, *4* (8), 7487−7491.

(13) Kim, S.; Yin, L.; Bak, S. M.; Fister, T. T.; Park, H.; Parajuli, P.; Gim, J.; Yang, Z.; Klie, R. F.; Zapol, P.; Du, Y.; Lapidus, S. H.; Vaughey, J. T. Investigation of Ca Insertion into α-MoO_3 Nanoparticles for High Capacity Ca-Ion Cathodes. *Nano Lett.* **2022**, *22* (6), 2228−2235.

(14) Wang, J.; Tan, S.; Xiong, F.; Yu, R.; Wu, P.; Cui, L.; An, Q. $VOPO_4{\cdot}2H_2O$ as a new cathode material for rechargeable Ca-ion batteries. *Chem. Commun.* **2020**, *56* (26), 3805−3808.

(15) Lipson, A. L.; Kim, S.; Pan, B.; Liao, C.; Fister, T. T.; Ingram, B. J. Calcium intercalation into layered fluorinated sodium iron phosphate. *J. Power Sources* **2017**, *369*, 133−137.
(16) Zhang, S.; Zhu, Y.; Wang, D.; Li, C.; Han, Y.; Shi, Z.; Feng, S. Poly(Anthraquinonyl Sulfide)/CNT Composites as High-Rate-Performance Cathodes for Nonaqueous Rechargeable Calcium-Ion Batteries. *Adv. Sci.* **2022**, *9* (14), No. e2200397.
(17) Qin, R.; Wei, Y.; Zhai, T.; Li, H. LISICON structured $Li_3V_2(PO_4)_3$ with high rate and ultralong life for low-temperature lithium-ion batteries. *J. Mater. Chem. A* **2018**, *6* (20), 9737−9746.
(18) Jin, T.; Li, H.; Zhu, K.; Wang, P.-F.; Liu, P.; Jiao, L. Polyanion-type cathode materials for sodium-ion batteries. *Chem. Soc. Rev.* **2020**, *49* (8), 2342−2377.
(19) Jeon, B.; Heo, J. W.; Hyoung, J.; Kwak, H. H.; Lee, D. M.; Hong, S.-T. Reversible Calcium-Ion Insertion in NASICON-Type $NaV_2(PO_4)_3$. *Chem. Mater.* **2020**, *32* (20), 8772−8780.
(20) Blanc, L. E.; Choi, Y.; Shyamsunder, A.; Key, B.; Lapidus, S. H.; Li, C.; Yin, L.; Li, X.; Gwalani, B.; Xiao, Y.; Bartel, C. J.; Ceder, G.; Nazar, L. F. Phase Stability and Kinetics of Topotactic Dual Ca^{2+}-Na^+ Ion Electrochemistry in NaSICON $NaV_2(PO_4)_3$. *Chem. Mater.* **2023**, *35* (2), 468−481.
(21) Chen, C.; Shi, F.; Zhang, S.; Su, Y.; Xu, Z. L. Ultrastable and High Energy Calcium Rechargeable Batteries Enabled by Calcium Intercalation in a NASICON Cathode. *Small* **2022**, *18* (14), 2107853.
(22) Kim, S.; Yin, L.; Lee, M. H.; Parajuli, P.; Blanc, L.; Fister, T. T.; Park, H.; Kwon, B. J.; Ingram, B. J.; Zapol, P.; Klie, R. F.; Kang, K.; Nazar, L. F.; Lapidus, S. H.; Vaughey, J. T. High-Voltage Phosphate Cathodes for Rechargeable Ca-Ion Batteries. *ACS Energy Lett.* **2020**, *5* (10), 3203−3211.
(23) Kim, H.; Choi, W.; Yoon, J.; Um, J. H.; Lee, W.; Kim, J.; Cabana, J.; Yoon, W.-S. Exploring anomalous charge storage in anode materials for next-generation Li rechargeable batteries. *Chem. Rev.* **2020**, *120* (14), 6934−6976.
(24) Zhang, Z.; Li, W.; Ng, T.-W.; Kang, W.; Lee, C.-S.; Zhang, W. Iron(ii) molybdate ($FeMoO_4$) nanorods as a high-performance anode for lithium ion batteries: structural and chemical evolution upon cycling. *J. Mater. Chem. A* **2015**, *3* (41), 20527−20534.
(25) Cao, B.; Liu, Z.; Xu, C.; Huang, J.; Fang, H.; Chen, Y. High-rate-induced capacity evolution of mesoporous C@SnO_2@C hollow nanospheres for ultra-long cycle lithium-ion batteries. *J. Power Sources* **2019**, *414*, 233−241.
(26) Zhang, Q.; Pei, J.; Chen, G.; Bie, C.; Sun, J.; Liu, J. Porous $Co_3V_2O_8$ Nanosheets with Ultrahigh Performance as Anode Materials for Lithium Ion Batteries. *Adv. Mater. Interfaces* **2017**, *4* (13), 1700054.
(27) Sun, H.; Xin, G.; Hu, T.; Yu, M.; Shao, D.; Sun, X.; Lian, J. High-rate lithiation-induced reactivation of mesoporous hollow spheres for long-lived lithium-ion batteries. *Nat. Commun.* **2014**, *5*, 4526.
(28) Su, L.; Zhou, Z.; Qin, X.; Tang, Q.; Wu, D.; Shen, P. $CoCO_3$ submicrocube/graphene composites with high lithium storage capability. *Nano Energy* **2013**, *2* (2), 276−282.
(29) Sun, M.; Zhang, H.; Wang, Y.-F.; Liu, W.-L.; Ren, M.-M.; Kong, F.-G.; Wang, S.-J.; Wang, X.-Q.; Duan, X.-L.; Ge, S.-Z. Co/CoO@N-C nanocomposites as high-performance anodes for lithium-ion batteries. *J. Alloy. Compd.* **2019**, *771*, 290−296.
(30) Ye, D.; Zeng, G.; Nogita, K.; Ozawa, K.; Hankel, M.; Searles, D. J.; Wang, L. Understanding the Origin of Li_2MnO_3 Activation in Li-Rich Cathode Materials for Lithium-Ion Batteries. *Adv. Funct. Mater.* **2015**, *25* (48), 7488−7496.
(31) Luo, J.; Liu, J.; Zeng, Z.; Ng, C. F.; Ma, L.; Zhang, H.; Lin, J.; Shen, Z.; Fan, H. J. Three-dimensional graphene foam supported Fe_3O_4 lithium battery anodes with long cycle life and high rate capability. *Nano Lett.* **2013**, *13* (12), 6136−6143.
(32) Sauvage, F.; Quarez, E.; Tarascon, J.-M.; Baudrin, E. Crystal structure and electrochemical properties vs. Na^+ of the sodium fluorophosphate $Na_{1.5}VOPO_4F_{0.5}$. *Solid State Sci.* **2006**, *8* (10), 1215−1221.
(33) Wang, J.; Tan, S.; Zhang, G.; Jiang, Y.; Yin, Y.; Xiong, F.; Li, Q.; Huang, D.; Zhang, Q.; Gu, L.; An, Q.; Mai, L. Fast and stable Mg^{2+} intercalation in a high voltage $NaV_2O_2(PO_4)_2F$/rGO cathode material for magnesium-ion batteries. *Sci. China Mater.* **2020**, *63* (9), 1651−1662.
(34) Guo, J.-Z.; Wang, P.-F.; Wu, X.-L.; Zhang, X.-H.; Yan, Q.; Chen, H.; Zhang, J.-P.; Guo, Y.-G. High-Energy/Power and Low-Temperature Cathode for Sodium-Ion Batteries: In Situ XRD Study and Superior Full-Cell Performance. *Adv. Mater.* **2017**, *29* (33), 1701968.
(35) Zhao, L.; Rong, X.; Niu, Y.; Xu, R.; Zhang, T.; Li, T.; Yu, Y.; Hou, Y. Ostwald Ripening Tailoring Hierarchically Porous $Na_3V_2(PO_4)_2O_2F$ Hollow Nanospheres for Superior High-Rate and Ultrastable Sodium Ion Storage. *Small* **2020**, *16* (48), 2004925.
(36) Xu, J.; Chen, J.; Tao, L.; Tian, Z.; Zhou, S.; Zhao, N.; Wong, C.-P. Investigation of $Na_3V_2(PO_4)_2O_2F$ as a sodium ion battery cathode material: Influences of morphology and voltage window. *Nano Energy* **2019**, *60*, 510−519.
(37) Wang, H.; Liu, F.; Yu, R.; Wu, J. Unraveling the reaction mechanisms of electrode materials for sodium-ion and potassium-ion batteries by in situ transmission electron microscopy. *Interdiscip. Mater.* **2022**, *1* (2), 196−212.
(38) Zuo, C.; Chao, F.; Li, M.; Dai, Y.; Wang, J.; Xiong, F.; Jiang, Y.; An, Q. Improving Ca-ion Storage Dynamic and Stability by Interlayer Engineering and Mn-dissolution Limitation Based on Robust MnO_2@PANI Hybrid Cathode. *Adv. Energy Mater.* **2023**, *13* (30), 2301014.
(39) Yu, R.; Pan, Y.; Jiang, Y.; Zhou, L.; Zhao, D.; Van Tendeloo, G.; Wu, J.; Mai, L. Regulating Lithium Transfer Pathway to Avoid Capacity Fading of Nano Si Through Sub-Nano Scale Interfused SiO_x/C Coating. *Adv. Mater.* **2023**, *35* (49), 2306504.
(40) Lou, S.; Liu, Q.; Zhang, F.; Liu, Q.; Yu, Z.; Mu, T.; Zhao, Y.; Borovilas, J.; Chen, Y.; Ge, M.; et al. Insights into interfacial effect and local lithium-ion transport in polycrystalline cathodes of solid-state batteries. *Nat. Commun.* **2020**, *11* (1), 5700.
(41) Qi, Y.; Tong, Z.; Zhao, J.; Ma, L.; Wu, T.; Liu, H.; Yang, C.; Lu, J.; Hu, Y.-S. Scalable Room-Temperature Synthesis of Multi-shelled $Na_3(VOPO_4)_2F$ Microsphere Cathodes. *Joule* **2018**, *2* (11), 2348−2363.
(42) Zhang, X.; Wei, H.; Ren, B.; Jiang, J.; Qu, G.; Yang, J.; Chen, G.; Li, H.; Zhi, C.; Liu, Z. Unlocking High-Performance Ammonium-Ion Batteries: Activation of In-Layer Channels for Enhanced Ion Storage and Migration. *Adv. Mater.* **2023**, *35* (40), No. e2304209.
(43) Deng, L.; Yu, F.-D.; Xia, Y.; Jiang, Y.-S.; Sui, X.-L.; Zhao, L.; Meng, X.-H.; Que, L.-F.; Wang, Z.-B. Stabilizing fluorine to achieve high-voltage and ultra-stable $Na_3V_2(PO_4)_2F_3$ cathode for sodium ion batteries. *Nano Energy* **2021**, *82*, 105659.
(44) Ni, Q.; Jiang, H.; Sandstrom, S.; Bai, Y.; Ren, H.; Wu, X.; Guo, Q.; Yu, D.; Wu, C.; Ji, X. A $Na_3V_2(PO_4)_2O_{1.6}F_{1.4}$ Cathode of Zn-Ion Battery Enabled by a Water-in-Bisalt Electrolyte. *Adv. Funct. Mater.* **2020**, *30* (36), 2003511.
(45) Yu, M.; Sui, Y.; Sandstrom, S. K.; Wu, C. Y.; Yang, H.; Stickle, W.; Luo, W.; Ji, X. Reversible Copper Cathode for Nonaqueous Dual-Ion Batteries. *Angew. Chem., Int. Ed.* **2022**, *61* (47), No. e202212191.
(46) Wang, J.; Li, X.; Wang, Z.; Guo, H.; Huang, B.; Wang, Z.; Yan, G. Systematic investigation on determining chemical diffusion coefficients of lithium ion in $Li_{1+x}VPO_4F$ ($0 \leq x \leq 2$). *J. Solid State Electrochem.* **2015**, *19*, 153−160.
(47) Shulga, Y. M.; Tien, T.-C.; Huang, C.-C.; Lo, S.-C.; Muradyan, V. E.; Polyakova, N. V.; Ling, Y.-C.; Loutfy, R. O.; Moravsky, A. P. XPS study of fluorinated carbon multi-walled nanotubes. *J. Electron Spectrosc. Relat. Phenom.* **2007**, *160* (1−3), 22−28.
(48) Hwang, J.; Matsumoto, K.; Hagiwara, R. Electrolytes toward High-Voltage $Na_3V_2(PO_4)_2F_3$ Positive Electrode Durable against Temperature Variation. *Adv. Energy Mater.* **2020**, *10* (34), 2001880.
(49) Wang, K.; Li, H.; Guo, G.; Zheng, L.; Passerini, S.; Zhang, H. Enabling Multi-electron Reactions in NASICON Positive Electrodes for Aqueous Zinc-Metal Batteries. *ACS Energy Lett.* **2023**, *8* (4), 1671−1679.

https://doi.org/10.1021/acsnano.4c08704
ACS Nano 2024, 18, 28246−28257

(50) Lindström, H.; Södergren, S.; Solbrand, A.; Rensmo, H.; Hjelm, J.; Hagfeldt, A.; Lindquist, S.-E. Li^+ ion insertion in TiO_2 (anatase). 2. Voltammetry on nanoporous films. *J. Phys. Chem. B* **1997**, *101* (39), 7717−7722.
(51) Wang, J.; Polleux, J.; Lim, J.; Dunn, B. Pseudocapacitive contributions to electrochemical energy storage in TiO_2 (anatase) nanoparticles. *J. Phys. Chem. C* **2007**, *111* (40), 14925−14931.
(52) Shen, L.; Wang, Y.; Lv, H.; Chen, S.; van Aken, P. A.; Wu, X.; Maier, J.; Yu, Y. Ultrathin $Ti_2Nb_2O_9$ nanosheets with pseudocapacitive properties as superior anode for sodium-ion batteries. *Adv. Mater.* **2018**, *30* (51), 1804378.

https://doi.org/10.1021/acsnano.4c08704
ACS Nano 2024, 18, 28246−28257